

REVIEW

A polarimetric Doppler radar time-series simulator for biological applications

Phillip M. Stepanian^{1,2}, Djordje Mirkovic³ & Phillip B. Chilson⁴¹Radar Entomology Unit, Computational and Analytical Sciences Department, Rothamsted Research, Harpenden Hertfordshire AL5 2JQ, United Kingdom²Corix Plains Institute, University of Oklahoma, Norman, Oklahoma 73019, USA³Cooperative Institute for Mesoscale Meteorological Studies, University of Oklahoma, Norman, Oklahoma 73072, USA⁴School of Meteorology, Advanced Radar Research Center, Center for Autonomous Sensing and Sampling, University of Oklahoma, Norman, Oklahoma 73072, USA**Keywords**

Aeroecology, agent-based modelling, individual-based modelling, polarimetry, simulation, weather surveillance radar

Correspondence

Phillip M. Stepanian, Corix Plains Institute, University of Oklahoma, Norman, Oklahoma 73019.

Tel: 405 325 4034; Fax: 405 325 7702;

E-mail: phillip.stepanian@gmail.com

Funding Information

This work was supported by a Marshall Sherfield Fellowship, the National Institute for Food and Agriculture of the U.S. Department of Agriculture under Award 2013-67009-20369 and the U.S. National Science Foundation under Grant EF-1340921.

Editor: Ned Horning

Associate Editor: Clare Duncan

Received: 13 November 2017; Revised: 19 February 2018; Accepted: 27 February 2018

doi: 10.1002/rse2.80

Remote Sensing in Ecology and Conservation 2018; **4** (4):285–302

Abstract

The high mobility of airborne organisms makes them inherently difficult to study, motivating the use of radars and radar networks as biological surveillance tools. While the utility of radar for ecological studies has been demonstrated, a number of challenges remain in expanding and optimizing their use for surveillance of birds, bats and insects. To explore these topics, a Lagrangian simulation scheme has been developed to synthesize realistic, polarimetric, pulsed Doppler radar baseband signals from modelled flocks of biological point scatterers. This radar simulation algorithm is described, and an application is presented using an agent-based model of the nocturnal emergence of a cave-dwelling colony of Brazilian free-tailed bats (*Tadarida brasiliensis*). Dual-polarization radar signals for an S-band weather surveillance radar are synthesized and used to develop a new extension of the spectral velocity azimuth display for polarimetric roost-ring signature analysis, demonstrating one capability of this simulation scheme. While these developments will have direct benefits for radar engineers and meteorologists, continuing investment in radar methods such as these will have cascading effects toward improving ecological models and developing new observational techniques for monitoring aerial wildlife.

Introduction

The study of birds, bats and insects in their atmospheric habitat is an expansive area of research, making use of many measurement, modelling and analysis techniques (Kunz et al. 2008; Bridge et al. 2011). A need for long-term, large-scale and high-resolution surveillance of the airspace has motivated application of radar as an

ecological measurement tool (Gauthreaux and Belser 2003), and potential use of existing networked weather radar infrastructure for real-time animal monitoring has spurred research efforts across the US (Chilson et al. 2012) and Europe (Shamoun-Baranes et al. 2014; Bauer et al. 2017). While ecological radar surveillance techniques continue to develop, parallel research programmes are approaching the topic of animal movements from a

modelling perspective (Grimm et al. 2005). In an effort to understand interactions among airborne organisms and changes in their aerial and terrestrial ecosystems, ecological models have been developed to simulate animal abundance, behaviour, distribution and movement as a function of their environment and surroundings (Erni et al. 2005; Shamoun-Baranes et al. 2010; McLane et al. 2011; Shamoun-Baranes and van Gasteren 2011; Bauer and Klaassen 2013). These biological modelling techniques have diagnostic value in identifying drivers of animal behaviour and movement, and also present future potential for prognostic applications in forecasting abundance and distributions of organisms (Clark et al. 2001; Shamoun-Baranes et al. 2010).

Although both ecological modelling and radar measurements have been applied in biological studies, no framework currently exists for generating realistic radar products from ecological models. The radar manifestation of objects in the airspace is a complicated combination of physical effects, including propagation, refraction and scattering of electromagnetic waves, as well as artefacts of radar hardware and sampling scheme. The combination of these effects and their net influence on the final radar observations is known generally as the 'forward process'. The combination of mathematical computations that relate objects in the airspace to their radar manifestation is commonly termed the 'forward operator' (Jung et al. 2008a). The task of synthesizing realistic radar observations from a defined set of aerial objects relies on defining a forward operator that emulates the forward process. The value of such a comparison technique has been demonstrated many times in meteorological applications in which atmospheric model output are related to remote-sensing measurements, providing model validation or physical interpretation of measurements (e.g. Zrnić 1975; Muschinski et al. 1999; Cheong et al. 2008; Jung et al. 2008a,b, 2010; Scipión et al. 2008; Ryzhkov et al. 2011; Wainwright et al. 2014; Byrd et al. 2016).

While the forward process converts aerial scatterers to radar signals, the 'backward' or 'retrieval' process attempts the reverse – relating radar signals to the identity of their underlying scatterers – and is the ultimate goal in most radar applications. Linking radar measurements to the taxonomic composition and behaviour of organisms aloft is still a major challenge, and often only possible when geography, phenology, or other prior knowledge can be used to deduce the likely occupants of the airspace (e.g. Horn and Kunz 2008; Frick et al. 2012; Melnikov et al. 2015). Nonetheless, these specialized cases (e.g. Leskinen et al. 2011) help illustrate capabilities of radar in movement modelling. Beyond the value in validating ecological models, simulating radar signals from a set of

known biological scatterers can enhance use of radar in ecological applications. This can include the ability to test different scanning strategies on a static distribution of scatterers, or development of biological radar retrieval algorithms using known model state as truth (Zrnić 1975). Moreover, the capability of linking – and eventually assimilating – radar measurements to a modelling framework could represent a step toward real-time ecological forecasting.

The major difficulty in simulating biological radar signals is that a parameterization framework (i.e. forward operator) such as those used in meteorological applications does not exist for biological scatterers. For example, rain is commonly parametrized using characteristic drop size distributions, stochastic spatial arrangements and canting angles, and the assumption of uniform beam filling (e.g. Straka et al. 2000; Ryzhkov et al. 2011). These rain characterizations can directly translate to Doppler moments at dual-polarizations using analytical or empirical expressions (Straka et al. 2000). The parallel for parameterizing animal behaviour and scattering characteristics directly into polarimetric radar products has only been attempted for widespread, homogenous, single-species migration (Melnikov et al. 2015). The practical implication to radar simulation is that no general links exist between Eulerian animal movement models and radio scattering characteristics, making Lagrangian techniques the only available option for calculations. Furthermore, because animal flight behaviour can vary erratically over small spatial scales, simplified Lagrangian methods that use a small subset of scatterers to stochastically represent the full collection (e.g. Vivekanandan et al. 1991) are not applicable. The only remaining method is a brute-force Lagrangian calculation in which all organisms within the radar sampling volume are treated as individual point scatterers and contribute to the final synthesized radar signals. As a first attempt toward a forward operator that converts ecological models into radar measurements, a computational framework for synthesizing polarimetric, pulsed-Doppler, baseband radar signals is developed.

Notation and Coordinate Transformations

For the following discussion, the term 'agent' will be used to describe a modelled biological point scatterer (i.e. bird, bat or insect) within a three-dimensional aerial domain. As such, the instantaneous state of an agent can be described by its position, velocity and orientation within the modelled airspace. It is assumed that some technique (e.g. an ecological model) has produced a series of such information for a total of N agents across M time steps.

The ultimate goal is to relate these native model output fields to quantities that are more relevant to radar measurements. Though conceptually simple, defining an agent's state with respect to a radar requires computations within and across several coordinate systems, often leading to notational difficulties. In an effort to avoid ambiguities, the following defines the notation of these coordinate systems, and sequential transformations through them. A table of symbols and notation is provided in Appendix 1.

As a general starting point, it is assumed that the format of the ecological model output describes the geographical position of the i th agent at the t th time step as

$$\mathbf{X}_{\text{geo}}(i, t) = \langle \text{lon}(i, t), \text{lat}(i, t), \text{alt}(i, t) \rangle \quad (1)$$

using degrees longitude (lon), degrees latitude (lat) and altitude in metres above mean sea level (alt). Similarly, the instantaneous motion of an agent is described as

$$\mathbf{V}(i, t) = \langle u(i, t), v(i, t), w(i, t) \rangle \quad [\text{m sec}^{-1}] \quad (2)$$

where u , v and w represent the agent's zonal, meridional and vertical velocity components respectively (Fig. 1B). Thus, the ecological model output consists of two arrays – position and velocity – each with size $(N \times M \times 3)$. Starting from these native output arrays, it is first necessary to define the desired location of the simulated radar:

$$\mathbf{X}_{\text{geo,rad}} = \langle \text{lon}_{\text{rad}}, \text{lat}_{\text{rad}}, \text{alt}_{\text{rad}} \rangle \quad (3)$$

Once this radar location has been designated, a Cartesian coordinate system is defined with the radar at the origin, the positive \hat{X} -axis pointing east, the positive \hat{Y} -axis pointing north and the positive \hat{Z} -axis pointing opposite the force of gravity (Fig. 1A). The agent position

array is transformed onto this radar-centred coordinate system

$$\mathbf{X}_{\text{cart}}(i, t) = \langle x(i, t), y(i, t), z(i, t) \rangle \quad (4)$$

through the geodetic relations

$$x = (\text{lon} - \text{lon}_{\text{rad}}) \frac{a \pi \cos(\text{lat})}{180^\circ [1 - e^2 \sin^2(\text{lat})]^{1/2}} \quad [\text{m}] \quad (5a)$$

$$y = 111\,200(\text{lat} - \text{lat}_{\text{rad}}) \quad [\text{m}] \quad (5b)$$

$$z = \text{alt} - \text{alt}_{\text{rad}} \quad [\text{m}] \quad (5c)$$

in which a is the ellipsoidal Earth's major axis radius in metres and e is eccentricity (Rapp 1991). In the 1984 World Geodetic System, these values are $a = 6\,378\,137.0$ m and $e = 0.081819$ (National Imagery and Mapping Agency, 1997).

Following this coordinate transformation, the Cartesian agent location array $\mathbf{X}_{\text{cart}}(i, t)$ implicitly assumes that the Earth is flat. In other words, agent positions take the x - y plane as the Earth surface, with z representing height above the radar. In this system, the radar beam path is subject to two distorting effects: perceived upward propagation due to curvature of the Earth, and radio refraction due to inhomogeneities in fields of pressure, temperature and humidity (Doviak and Zrnić 1993). Within the simulation framework, it is more computationally efficient to consider radar beams that follow ray geometry (i.e. straight-line propagation paths). Use of ray paths enables trigonometric calculations for describing the position of the beam and resolution volumes. To allow this geometry, the combined effect of these two sources of beam deformation are calculated and accounted for by

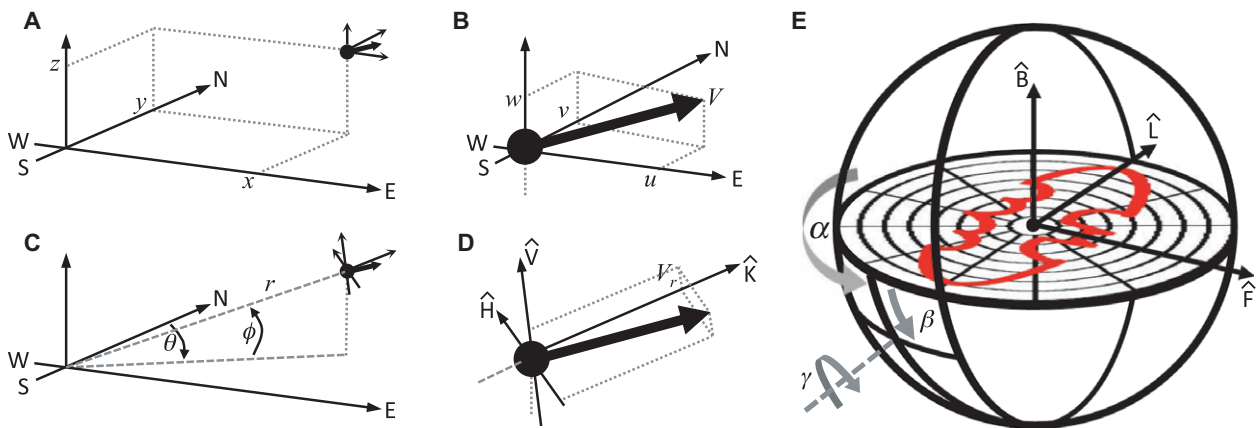


Figure 1. Coordinate system definitions: (A) The radar-centred cartesian coordinate system. (B) Blowup of agent location in (A) showing velocity components. (C) The radar-centred spherical coordinate system. (D) Blowup of agent location in (C) showing the projection of the velocity vector onto the 'ray' coordinate basis. (E) Details of the agent position in (D), showing orientation angle definitions.

'pre-distorting' the position of all agents in space with respect to the radar. In the original radar-centred coordinates, agent location with respect to the surface is defined by the surface arc distance from the radar ($s = \sqrt{x^2 + y^2}$) and height above ground level (z), while the position with respect to the radar beam is defined by slant range (r) and distance from boresight vector (d). These four values are identical for both round and flat Earth models in which the beam travels in non-linear paths (Fig. 2A and B, respectively). The radar measurement of an agent depends on its position with respect to the beam (i.e. r and d), and since the simulated radar measurement must not be affected by our choice of coordinate system, beam-relative agent positions must be identical after transformation to ray geometry. To achieve these conditions, the surface-relative positions of agents (i.e. x , y and z) are modified such that they create identical beam-relative positions for straight-line beam propagation (Fig. 2C). If a specific altitudinal refractivity gradient is to be emulated, a so-called equivalent Earth radius scaling parameter (k_e) can be calculated using

$$k_e = \frac{1}{1 + a \left(\frac{dn}{dz} \right)} \quad (6)$$

with $\frac{dn}{dz}$ being change in refractive index with height (Schelleng et al. 1933). Under these refractive conditions and for a given antenna elevation angle (ϕ_{pt}), beam height above antenna level (h) as a function of surface arc distance from the radar (s) can be computed for values of k_e using

$$h = \sqrt{r^2 + (k_e a)^2} + 2k_e a \arcsin(\phi_{pt}) - k_e a \quad [\text{m}] \quad (7a)$$

$$s = k_e a \arcsin\left(\frac{r \cos(\phi_{pt})}{k_e a + h}\right) \quad [\text{m}] \quad (7b)$$

as illustrated in Figure 2B (Doviak Zrnić 1993). Conversely, in simple ray geometry

$$h' = r \sin(\phi_{pt}) \quad [\text{m}] \quad (8a)$$

$$s' = r \cos(\phi_{pt}) \quad [\text{m}] \quad (8b)$$

as in Figure 2C. Using these relations, modified agent locations $\langle x', y', z' \rangle$ are defined to account for ray departure due to refraction and surface curvature. In this distorted Cartesian system, the radar beam is subject to ray geometry across a flat Earth, while retaining the same relative positions of scatterers with respect to the beam. Hereafter the Cartesian system $\mathbf{X}_{\text{cart}}(i, t)$ will refer to agent positions that have been pre-distorted to account for Earth curvature and beam refraction, and the prime notation will be omitted (Fig. 1A).

The resulting Cartesian agent location array $\mathbf{X}_{\text{cart}}(i, t)$ is converted into radar-centred spherical coordinates

$$\mathbf{X}_{\text{sph}}(i, t) = \langle r(i, t), \phi(i, t), \theta(i, t) \rangle \quad (9)$$

using

$$r = \sqrt{x^2 + y^2 + z^2} \quad [\text{m}] \quad (10a)$$

$$\phi = \arcsin\left(\frac{z}{r}\right) \quad [\text{deg}] \quad (10b)$$

$$\theta = \arctan2(x, y) \quad [\text{deg}] \quad (10c)$$

with ϕ denoting elevation angle in degrees above the horizon, θ denoting azimuth angle in degrees clockwise from north and $\arctan2(\cdot)$ denoting the four-quadrant inverse tangent. The result of these transformations is an array of three-dimensional agent positions in the radar-relative spherical coordinates that are common in radar applications (Fig. 1C).

A similar procedure is needed to produce the final two quantities relevant to polarimetric Doppler radar measurements, namely, radial velocity and radar-relative orientation. Because both of these quantities are dependent on the position and velocity of the agent with respect to the radar beam, it is convenient to introduce two additional coordinate bases to describe these quantities. Following notation presented in Brangi and Chandrasekar (2001), the first system is centred on the agent with the positive \hat{K} -axis pointing radially away from the radar, the positive \hat{H} -axis pointing to the left of the radial vector and parallel to the ground and the \hat{V} -axis completing the orthogonal, right-hand coordinate basis (Fig. 1D). Describing this 'ray' system in terms of common polarimetric radar language, \hat{H} is the horizontal polarization axis, \hat{V} is the vertical polarization axis and \hat{K} is the radial axis of an incident beam directed at the agent.

The second system is centred on the agent's body, in constant alignment with the agent's orientation. In this case, orientation is defined based on the agent's motion under the assumption that each agent is oriented head-first along the horizontal component of its velocity vector with the body and both wings parallel with the horizon. In other words, while an agent may climb or turn, inflight orientation will not include pitch or roll – only yaw. As a result, this Cartesian 'body' system is oriented with the positive \hat{F} -axis pointing forward along the agent's horizontal velocity vector, the positive \hat{L} -axis pointing to the agent's left wing and parallel to the ground, and the \hat{B} -axis emanating out of the agent's back, completing the orthogonal, right-hand coordinate basis (Fig. 1E).

Following these definitions, an agent's radial velocity, V_r , is the projection of the native velocity vector, $\mathbf{V}(i, t)$,

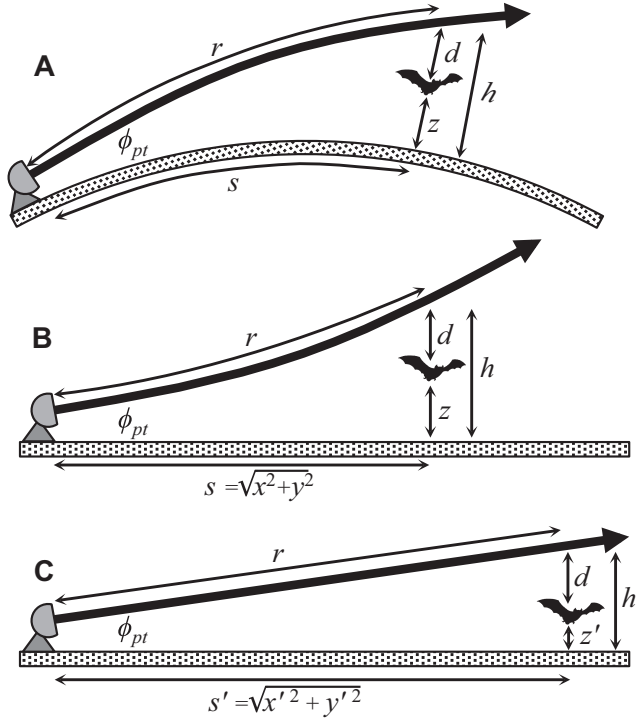


Figure 2. Relation between the Earth surface, agent position and beam geometry for (A) round Earth with beam refraction, (B) flat Earth with beam refraction and (C) flat Earth with ray beam geometry that maintains beam-relative agent positions.

onto the \hat{K} axis, and can be calculated using the rotation relation

$$V_r(i, t) = -u \sin(\theta) \sin(\phi) - v \cos(\theta) \sin(\phi) + w \cos(\phi) \quad (11)$$

based on agent position angles found in (10b,c). Radar-relative orientation can be described in terms of angular differences between the ‘ray’ and ‘body’ coordinate systems. This orientation with respect to the radar beam is found using three Euler angles that define three rotations of the agent’s ‘body’ frame to final alignment with the radar ‘ray’ frame. In successive order, these rotations are: $\alpha \equiv$ rotation around the \hat{B} -axis (i.e. heading or yaw), turning to the agent’s left, and yielding the new ‘prime body’ coordinates, $\hat{F}'\hat{L}'\hat{B}'$.

$\beta \equiv$ rotation around the \hat{L}' -axis (i.e. elevation or pitch), with the head rising and tail dropping, and yielding the new ‘double-prime body’ coordinates, $\hat{F}''\hat{L}''\hat{B}''$.

$\gamma \equiv$ rotation around the \hat{F}'' -axis (i.e. bank or roll), with the right wing dropping and left wing rising, and resulting in the alignment with the ‘ray’ coordinates, $\hat{K}\hat{H}\hat{V}$.

By imposing level inflight orientation, radar-relative orientation will only require α and β , with γ always

assuming a value of zero. Following conventions shown in Figure 1E, these angles are calculated using

$$\alpha = \text{sgn}(-u \cos(\theta) + v \sin(\theta)) \dots \arccos\left(\frac{xu + yv}{\sqrt{x^2 + y^2} \sqrt{u^2 + v^2}}\right) \quad [\text{deg}] \quad (12a)$$

$$\beta = -\phi \quad [\text{deg}] \quad (12b)$$

with $\text{sgn}(\cdot)$ denoting the signum function. The result of these transformations are three new arrays that describe the position $\langle r, \phi, \theta \rangle$, velocity $\langle V_r \rangle$ and orientation $\langle \alpha, \beta \rangle$ of agents in terms that are most relevant to polarimetric Doppler radar.

Radar Signal Synthesis for a Single Pulse

To simplify this initial formulation of the radar signal, only a single transmitted pulse will be considered. This will eliminate the need to consider pulse-to-pulse motion of agents and mechanical scanning of the radar beam. Building upon these results, the following section formulates the full algorithm that considers beam and agent motions.

Defining the radar system

With only the position of the radar currently defined, it is necessary to specify the characteristics of the radar system. For a single transmitted pulse, several specifications are required: radar wavelength (λ , [m]), transmit power (P_t , [W]), pulse width (τ , [s]), receiver sample time (τ_s , [s]), antenna beam pattern (f), antenna gain (G), initial transmit phases at horizontal and vertical polarizations ($\psi_{t,h}$ and $\psi_{t,v}$, [deg]), and system phase shifts on reception ($\psi_{r,h}$ and $\psi_{r,v}$, [deg]). Additionally, radar pointing direction (i.e. boresight) must be specified by the antenna elevation angle (ϕ_{pt}) and azimuth (θ_{pt}).

When an existing radar system is to be emulated, it is often possible to obtain the precise specifications of the system (e.g. a measured antenna beam pattern). However, when such information are not available, or when testing hypothetical radar designs, generalized expressions may be used. For example, Doviak and Zrnić (1993) provide a functional expression for the one-way beam weighting pattern for a circularly symmetric beam of a given beam-width (ϑ_b) as

$$f^2(\vartheta) = \left\{ \frac{8J_2[(1.27\pi \sin \vartheta)/\vartheta_b]}{[(1.27\pi \sin \vartheta)/\vartheta_b]^2} \right\}^2 \quad (13)$$

where ϑ is angular distance off of boresight in radians, and $J_2(\cdot)$ denotes a second order Bessel function. Similarly, the range weighting function ($|W(r, r_o)|$) can be represented, assuming a Gaussian transfer function, as

$$|W(r, r_o)| = [\text{erf}(x + b) - \text{erf}(x - b)]/2 \quad (14)$$

in which

$$\begin{aligned} b &= B\tau\pi/4\sqrt{\ln 2} \\ x &= 2aB/c(r_o - r) \\ a &= \pi/2\sqrt{\ln 2} \end{aligned} \quad (15)$$

with r_o being location of the centre of the nominal range gate [m], B representing receiver bandwidth and $\text{erf}(\cdot)$ denoting the error function (Doviak and Zrnić 1993).

The combination of beam and range weighting functions defines the resolution (i.e. size) of the pulse sampling volumes, but their location in space is determined by ranges corresponding with receiver sample times. In other words, immediately following the transmitted pulse, a sample will be taken every τ_s sec, placing the centre of a resolution volume every $c\tau_s/2$ m along the ray. This mapping between range and time provides the link between the time-series data stream that will be synthesized and the location of each nominal range gate in space, such

that the n th sample following the transmitted pulse corresponds to a distance

$$r_o(n) = \frac{cn\tau_s}{2} \quad [\text{m}] \quad (16)$$

with c representing the speed of light [m sec^{-1}]. Combined with the two boresight angles (ϕ_{pt}, θ_{pt}), $r_o(n)$ provides the spatial coordinates for the centre of each resolution volume for the n time-series samples following the transmitted pulse.

Organizing calculations for dual-polarizations

The defining characteristic of polarimetric radar is transmission and reception of radiation of diverse polarizations – in this case, horizontal and vertical. The method of sequestering these signals upon transmission and reception can be conducted simultaneously or alternately. The following formulation will consider Simultaneous Transmission and Simultaneous Reception (STSR) because this mode of operation can produce polarimetric information with a single pulse. This formulation can be extended to Alternating Transmission and Simultaneous Reception (ATSR) or Alternating Transmission and Alternating Reception (ATAR) modes by performing calculations for each polarization separately.

Determining scattering characteristics

Two factors are important for characterizing organismal radio scatter: radar cross section (σ_b) and backscatter phase (ψ_s). Both quantities vary with orientation of the animal with respect to the radar (α, β, γ), as well as polarization. As a result, a given animal can be defined at a specified wavelength by the incident and scattered polarization components of backscattered cross section and phase at each view angle relative to the radar:

$$\begin{bmatrix} \sigma_{b,hh}(\alpha, \beta, \gamma) & \sigma_{b,hv}(\alpha, \beta, \gamma) \\ \sigma_{b,vh}(\alpha, \beta, \gamma) & \sigma_{b,vv}(\alpha, \beta, \gamma) \end{bmatrix} \quad (17)$$

and

$$\begin{bmatrix} \psi_{s,hh}(\alpha, \beta, \gamma) & \psi_{s,hv}(\alpha, \beta, \gamma) \\ \psi_{s,vh}(\alpha, \beta, \gamma) & \psi_{s,vv}(\alpha, \beta, \gamma) \end{bmatrix} \quad (18)$$

(Melnikov et al. 2015).

At present, studies of organismal radio-wave scattering have rarely focused on dual-polarizations or phase contributions, and generally only present radar cross section at the horizontal polarization (see Vaughn 1985 for a

review). Much of this work has focused on direct radio measurements of specimens in a laboratory setting; however, no work to date has presented such polarimetric measurements of both amplitude and phase from lateral viewing angles. The most promising alternative source of these scattering data is from electromagnetic modelling efforts that use theoretical calculations to characterize the amplitude and phase of animal backscatter. In most existing studies, polarimetric power analysis has been conducted to explain differential reflectivity observations (e.g. Mueller and Larkin 1985; Wilson et al. 1994; Lang et al. 2004; Hobbs and Aldhous 2006), but few have modelled scattering phase (Zrnić and Ryzhkov 1998; Melnikov et al. 2015; Mirkovic et al. 2016). These latter exceptions that present both scattered amplitude and phase fall into two categories. Studies by Melnikov et al. (2015) and Zrnić and Ryzhkov (1998) apply general scattering calculations, modelling insects and birds as prolate spheroids, and thus produce polarimetric scattering properties at a variety of viewing angles. Work by Mirkovic et al. (2016) uses the method of moments on a specialized anatomical model of a bat to calculate the scattering amplitude and phase at dual-polarizations. Such modelling efforts represent the ideal method for producing the scattering characteristics required for assimilation into this radar simulation framework.

Calculating echo amplitude and phase

Using the radar system and scattering characteristic definitions above, and assuming that half of the total transmit power is allocated to each polarization, the STSR power contributions from the i th agent for the n th sample following a single transmitted pulse are calculated using the radar range equation for point scatterers,

$$P_{r,hh,i}(n) = \frac{P_t G^2 \lambda^2 \sigma_{b,hh,i} f^4(\vartheta_i) |W^2(r_i, r_o)|}{2(4\pi)^3 r_i^4} \quad (19a)$$

$$P_{r,hv,i}(n) = \frac{P_t G^2 \lambda^2 \sigma_{b,hv,i} f^4(\vartheta_i) |W^2(r_i, r_o)|}{2(4\pi)^3 r_i^4} \quad (19b)$$

$$P_{r,vh,i}(n) = \frac{P_t G^2 \lambda^2 \sigma_{b,vh,i} f^4(\vartheta_i) |W^2(r_i, r_o)|}{2(4\pi)^3 r_i^4} \quad (19c)$$

$$P_{r,vv,i}(n) = \frac{P_t G^2 \lambda^2 \sigma_{b,vv,i} f^4(\vartheta_i) |W^2(r_i, r_o)|}{2(4\pi)^3 r_i^4} \quad (19d)$$

in which ϑ_i is angular distance of the i th scatterer off the centre of the beam axis and $\sigma_{b,i}(\alpha, \beta)$ is radar cross section at the given transmission and reception polarizations,

corresponding with the agent's current orientation (as discussed in the previous section (Skolnik 2001)). The associated echo phase contributions from the i th agent are defined as

$$\psi_{i,hh} = \frac{4\pi r_i}{\lambda} + \frac{4\pi T_s}{\lambda} V_{r,i} + \psi_{s,hh,i} + \psi_{t,h} + \psi_{r,h} \quad (20a)$$

$$\psi_{i,hv} = \frac{4\pi r_i}{\lambda} + \frac{4\pi T_s}{\lambda} V_{r,i} + \psi_{s,hv,i} + \psi_{t,v} + \psi_{r,h} \quad (20b)$$

$$\psi_{i,vh} = \frac{4\pi r_i}{\lambda} + \frac{4\pi T_s}{\lambda} V_{r,i} + \psi_{s,vh,i} + \psi_{t,h} + \psi_{r,v} \quad (20c)$$

$$\psi_{i,vv} = \frac{4\pi r_i}{\lambda} + \frac{4\pi T_s}{\lambda} V_{r,i} + \psi_{s,vv,i} + \psi_{t,v} + \psi_{r,v} \quad (20d)$$

using radial velocity ($V_{r,i}$) and scatter phase ($\psi_{s,i}(\alpha, \beta)$) of the i th agent (Doviak and Zrnić 1993). Conceptually, each agent produces a contribution to the echo power and phase for each sample. The complex echo voltage contribution from the i th agent for the n th sample is calculated using in-phase and quadrature-phase components,

$$\begin{aligned} I_i(n) &= \sqrt{\frac{P_{r,i}(n)}{2}} \cos \psi_i \\ Q_i(n) &= \sqrt{\frac{P_{r,i}(n)}{2}} \sin \psi_i \\ V_i(n) &= I_i(n) + jQ_i(n) \end{aligned} \quad (21)$$

with j representing the imaginary unit (i.e. $\sqrt{-1}$).

Next, time-series components from each of the N agents are coherently summed to obtain the final radar time-series echo voltage for the given transmit and receive polarizations:

$$V(n) = \sum_{i=1}^N V_i(n). \quad (22)$$

In the case of ATAR operation, these calculations are only required for co-polar contributions, that is, $V_{hh}(n)$ and $V_{vv}(n)$. For STSR operation, the received signals are the coherent sums of co- and cross-polar contributions at each received polarization. As a result, these calculations must be computed for all four polarizations (V_{hh} , V_{hv} , V_{vh} and V_{vv}) and summed as,

$$\begin{aligned} V_H(n) &= V_{hh}(n) + V_{hv}(n) \\ V_V(n) &= V_{vv}(n) + V_{vh}(n). \end{aligned} \quad (23)$$

Finally, if desired, white noise can be added to the final time-series at a level defined by the user. The resulting synthesized time-series segments represent the n range-

time samples from a single STSR dual-polarized pulse along a ray.

Radar Signals for Realistic Sampling

The previous section describes synthesis of a single transmitted pulse, but typical scanning strategies require transmission and reception of many pulses, often directed at different regions of space. The process of synthesizing realistic radar data within this framework is primarily an exercise in bookkeeping – solving a relatively simple set of equations for several hundred thousand agents at four unique polarization combinations and coherently adding the results. It is also simple bookkeeping to keep track of agent locations, velocities and orientations with respect to the scanning beam boresight at every pulse. While conceptually easy, the process is computationally expensive, requiring large arrays to store the pertinent information.

Defining the radar system and scan

For the case of realistic sampling strategies, several more radar parameters must be specified that define the Volume Coverage Pattern (VCP). These parameters include the set of azimuth and elevation angles that the antenna will cover, the Pulse Repetition Time (PRT, [sec]), and antenna scanning rate (ω_r , [deg sec⁻¹]). Given the VCP, the antenna scanning rate dictates where the boresight is located at a given time. Combined with the PRT, the antenna pointing direction (ϕ_{pt} , θ_{pt}) can be defined for each pulse. With this pointing direction continuously updating in time, the set of equations from the previous section can be solved for each pulse, resulting in full volume coverage. Furthermore, by updating the antenna pointing direction for each PRT, realistic sampling results such as beam smearing are created (see Appendix C in Doviak and Zrnić 1993).

Temporal Interpolation

Additionally, pulse-to-pulse motion of agents must be considered as the radar samples the airspace. For an agent-based model with a temporal resolution on the order of 1 sec, the position, velocity and orientation of each agent is linearly interpolated to result in unique information content at each PRT. Effects of agent motions within the beam coupled with pulse-to-pulse boresight motions result in samples that vary in time at the PRT, yielding realistic Doppler spectra and correlation coefficients. Following all calculations, the resulting ray data can be organized into volume scans as a function of azimuth, elevation and range.

Illustrative Example

Overview and simulation inputs

The US national network of weather surveillance radars (NEXRAD) is a proven tool for monitoring colonies of Brazilian free-tailed bats (*Tadarida brasiliensis*) across the southwestern and south central US (e.g. Horn and Kunz 2008; Chilson et al. 2012; Frick et al. 2012), and Horn and Kunz (2008) provide a particularly good introduction to the ecology, agricultural significance and radar surveillance of the bats of this region. As a brief demonstration of radar simulation capabilities in a realistic application, we synthesize S-band radar signals for the dusk emergence and dispersion of a cave-dwelling Brazilian free-tailed bat colony.

Agent-based model

The first step before any radar simulation can be performed is producing a set of Lagrangian agents that will act as the scatterers and move through the radar domain. The behavioural simulator used in this example is based on the 'boid' model described by Reynolds (1987, 1999), and determines an agent's flight velocity by the position of surrounding individuals. From this method, a relatively simple set of behavioural attributes, or 'rules', defines the decision-making process of each agent as it moves through space and time. Use of a rule-based technique enables dynamical interactions among agents to emerge across a wide range of spatial and temporal scales. Inputs to the biological behavioural model were based on the BATOIDS agent-based model, which was designed specifically for emulating the emergence of Brazilian free-tailed bat colonies, in which primary behavioural rules include velocity matching and collision avoidance (Hallam et al. 2006). The total population of the colony was set to one hundred thousand agents. While this value is representative of many maternity roosts of free-tailed bats in central Texas, some colonies may have populations on the order of one million (Betke et al. 2008).

The model was initialized with all bats within the cave (below ground level) and they were allowed to exit at a set rate through a 10 m by 10 m hole at the surface, producing the columnar group formation characteristic of these emergences (Wilkins 1989). Additional rules were set to mimic the transition from emergence to dispersion flight modes at a set altitude of 1.5 km. The biological behavioural simulation presented in this example spans a full emergence event, lasting 35 min and having updates every second. A video of the full emergence simulation is included in the supplemental file (Video S1). Figure 3 shows four snapshots from the first 20 min of this

simulation, with time increasing from left to right. The top row of panels shows a projection of the location of all 100 000 agents onto a horizontal plane. The bottom row shows the projection of the agents onto a vertically oriented plane running west to east. Initially, bats exit the cave and gain altitude in a dense, columnar formation, reducing individual risk of predation (Fig. 3, left column). Risk of encountering aerial predators decreases away from the cave mouth, allowing bats to transition to a dispersion flight mode (beginning in Fig. 3, second column). More specifically, upon reaching 1.5 km in altitude, each individual is programmed to move away from the group's collective centre of mass while slowly descending toward the ground. These rules were chosen to create the basic diverging flight directions observed in these emergence events, and also resulted in the concentrations of individuals to the north and south of the cave. As the first individuals reach 1.5 km, they begin dispersing away from the group's centre of mass (i.e. flying primarily northward) and as a result, begin shifting the group's centre of mass northward. The centre of mass eventually passes north of the main emergence column, and individuals reaching 1.5 km begin dispersing to the south, now

shifting the centre of mass southward. This alternating preference for north-south flight trajectories is therefore a nuance of the specific behavioural rules, rather than any biologically meaningful behaviour. As the emergence column continues the transition, the horizontal projection begins to develop a hole in the centre of the group as bats diverge from the cave location. At the final stages of the emergence, bats descend to the height at which they forage for insects (Fig. 3, right column). While this visualization only captures overall group motion, complex behavioural dynamics are also occurring on much smaller scales as individuals interact to avoid collisions and modify their position within the group.

Scattering model

The complex scattering characteristics of each agent must be defined to describe the desired organism – here, the Brazilian free-tailed bat. We use the backscatter amplitudes and phases generated for a Brazilian free-tailed bat at S-band (10 cm) using a method of moments model implemented in the WIPL-D software environment (Mirakovic et al. 2016). Scattering values were calculated at

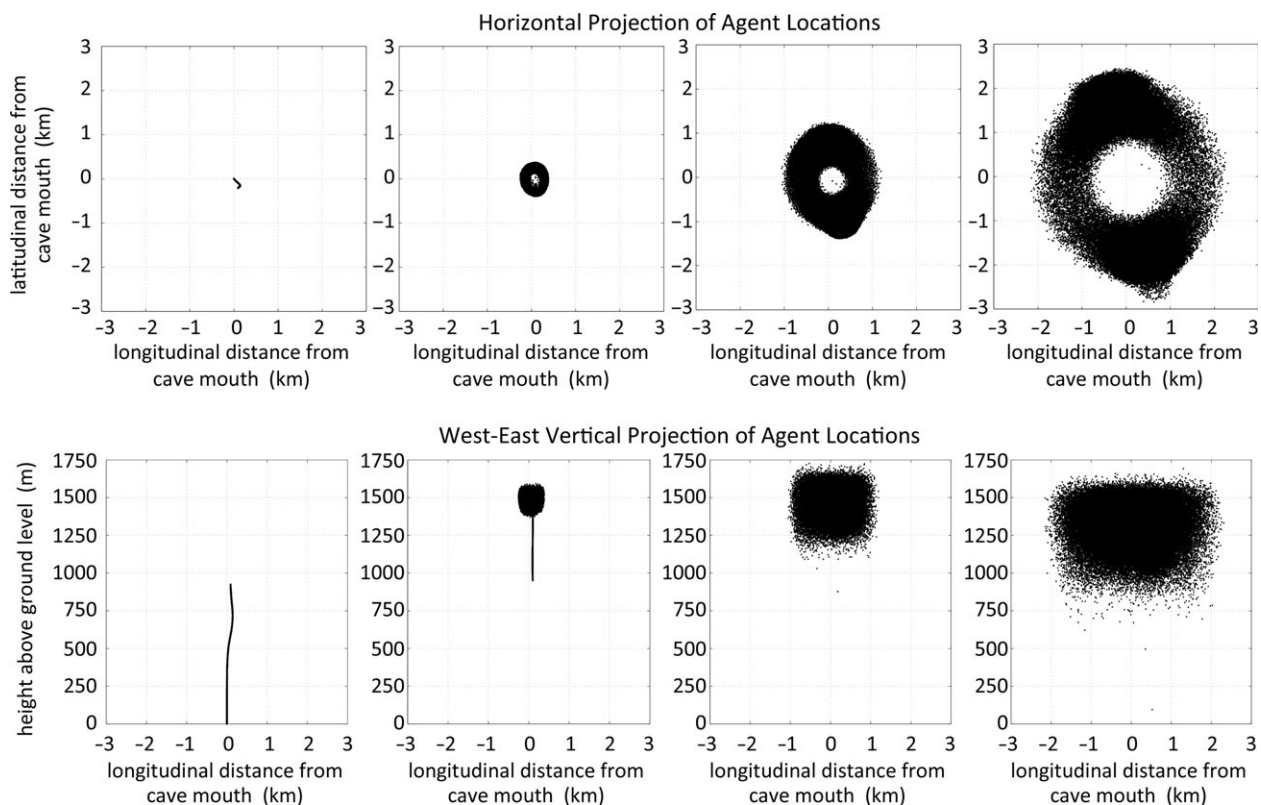


Figure 3. Biological behavioural model snapshots from 5, 10, 15 and 20 min into the simulation (left to right). The top row shows the horizontal projection of agent locations onto the ground. The bottom row shows the projection of agent locations onto a vertically oriented plane running west to east. Each point represents the location of a single agent (i.e. bat).

horizontal and vertical polarizations across all 4π steradians of possible viewing angles at 1° by 1° resolution.

Radar specifications and scanning strategy

Simulated radar specifications were selected to emulate a NEXRAD system (Doviak et al. 2000) running a specialized single-sweep, clear-air volume coverage pattern at a 1.5° -degree elevation angle. Radar system and scan specifications are listed in Table 1. Use of a single elevation sweep provides faster update times and avoids scanning altitudes above the expected flight ceiling for bats. The origin of the agent-based model was placed at ($x = 20$ km, $y = 20$ km) relative to the radar, such that the cave mouth was 28.28 km northeast of the radar site.

Simulation results

Using these radar specifications, the agent-based behavioural model, and the bat scattering characteristics, the simulation was run for the 35-min emergence event. The resulting dual-polarization baseband signals were processed into three conventional Doppler moments – reflectivity factor (Z_H), mean radial velocity (V_r) and spectrum width of radial velocity (σ_v) – using autocovariance processing (Doviak and Zrnić 1993, Section 6.4.1), as well as three standard NEXRAD polarimetric products – differential reflectivity (Z_{DR}), total differential phase (ψ_{DP}) and copolar correlation coefficient (ρ_{HV}) – following Doviak and Zrnić (1993, Section 6.8). A video of the time-evolution of all six radar products through the full emergence event is included in the supplemental file (Video S2). Figure 4 shows the radar products for four sweeps

corresponding with the snapshots presented in Figure 3. For context, we can compare these simulated products to actual radar observations of a dusk emergence of cave-dwelling bats – in this case, the Frio Cave bat colony as seen by the 0.5° elevation sweep of the Del Rio, Texas NEXRAD radar (KDFX; Fig. 5). The 0.5° sweep was chosen for comparison because Frio Cave is farther from the KDFX radar (61 km) than our modelled bat cave was from the simulated radar (28 km), and as a result, the 1.5° sweep would likely overshoot much of the bat population at Frio Cave. Modelled products in Figure 4D occur approximately at the same stage of the Frio Cave emergence shown in Figure 5B. In both cases, a ring-shaped pattern is evident in the reflectivity factor product, with the corresponding divergence signature in the radial velocity product that is characteristic of outward flights from a shared roost. Similar patterns of reflectivity factor and radial velocity can be seen for Purple Martin (*Progne subis*) flights, and are presented in Van Den Broeke (2013) and Stepanian et al. (2016). The variability of polarimetric products around the emergence ring indicates the variability of aspect viewing angles with respect to the radar site as individual headings are oriented away from the cave – a polarimetric signature common to roost exodus flights of birds and bats (Van Den Broeke 2013; Stepanian et al. 2016; Mirkovic et al. 2016). While many of these features of the real observations are emulated in the simulated results, many details are clearly not correct, indicating differences between our simulated bat colony and the colony at Frio Cave or deficiencies in our underlying behavioural model. For example, despite covering approximately the same spatial area, the simulated reflectivity factor (Fig. 4D) is much lower than observations of Frio Cave (Fig. 5D), indicating that more bats were occupying the airspace over Frio Cave than our simulated colony of 100 000 individuals. The radial velocity product of real observations indicates inbound flights reaching 12 m sec^{-1} (Fig. 5B), while our simulation has maximum radial velocity values around 6 m sec^{-1} . Similarly, the observed variance of radial velocity is higher in the observations than our simulations, with measured spectrum width values around 4 m sec^{-1} compared to our modelled values of approximately 2 m sec^{-1} . The implication is that our behavioural model needs higher flight speeds with greater spatial variability to yield results that match observations. Azimuthal patterns in polarimetric products are also different between modelled and observed fields, and have several possible sources of variability. As discussed in Melnikov et al. (2015), azimuthal patterns of polarimetric products depend highly on the radar system's differential phase on transmission ($\psi_{t,d}$) and reception ($\psi_{r,d}$). Because these values are not known for NEXRAD sites such as KDFX, we chose arbitrary

Table 1. Radar specifications and scanning strategy for simulation

Radar Parameter	Value
Radar wavelength (λ)	0.10 m
Transmit power (P_t)	$1 \times 10^6 \text{ W}$
Pulse width (τ)	$1.57 \times 10^{-6} \text{ sec}$
Receiver sample time (τ_s)	$1.57 \times 10^{-6} \text{ sec}$
Antenna beam pattern (f)	eq. 13, $\vartheta_b = 0.96^\circ$
Antenna gain (G)	45 dB
Pulse repetition time (T_s)	$1 \times 10^{-3} \text{ s}$
Antenna rotation rate (ω_r)	6.02 deg s^{-1}
Elevation angle (ϕ_{pt})	1.5°
Azimuth angles (θ_{pt})	$1^\circ - 360^\circ$
Polarization mode	STSR
Horizontally polarized transmit phase ($\psi_{t,h}$)	45°
Vertically polarized transmit phase ($\psi_{t,v}$)	0°
Horizontally polarized receive phase ($\psi_{r,h}$)	0°
Vertically polarized receive phase ($\psi_{r,v}$)	0°
Pulses per Azimuth	166
Volume update time	60 sec

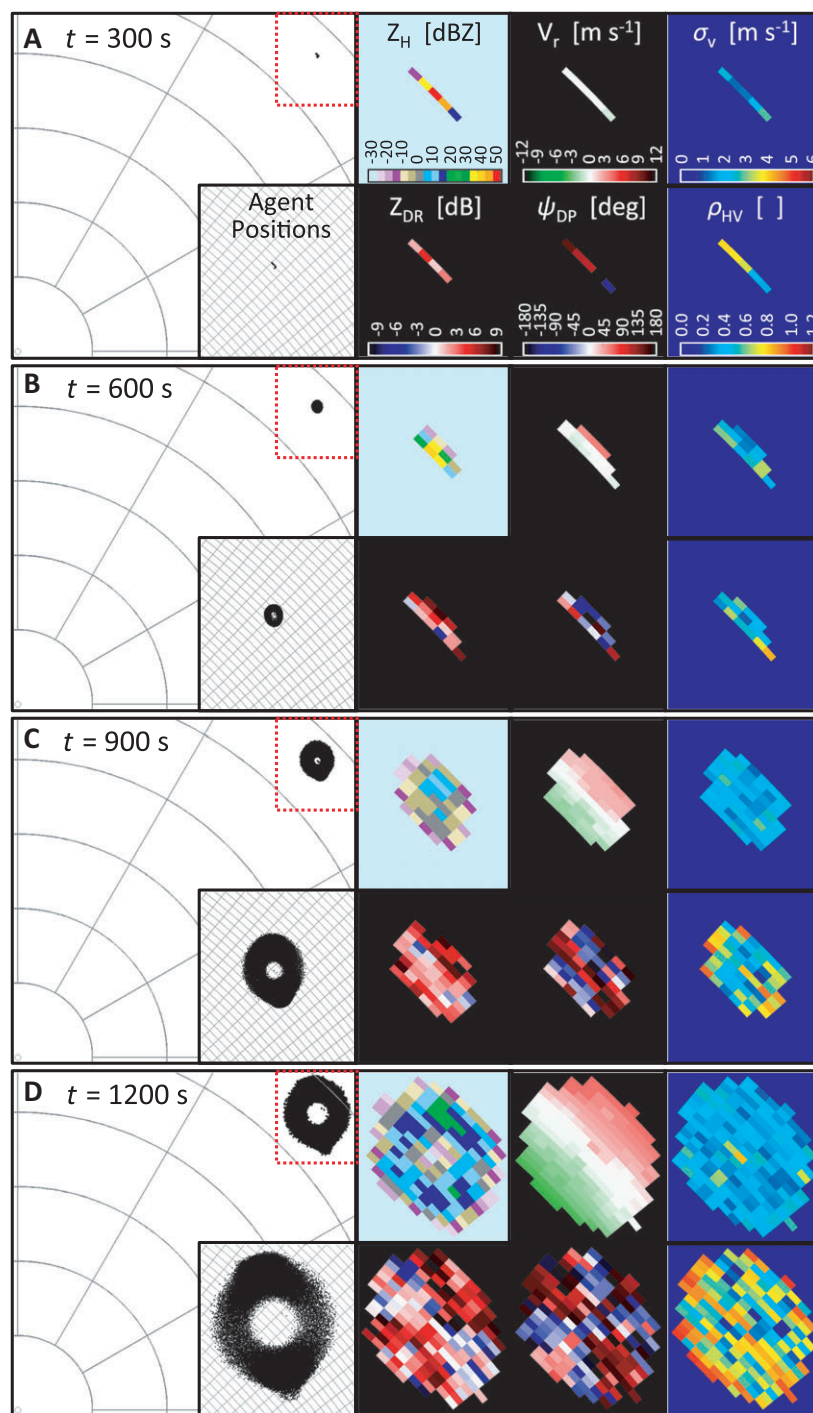


Figure 4. Synthesized radar products for the modelled bat emergence corresponding with the time steps shown in Figure 3. The red dotted boxes indicate the domain shown in the inset images. Colour scales in (A) are valid for all subplots. Range rings are spaced at 5-km increments.

values for both parameters (Table 1). Differences in these values between our simulation and KDFX may yield differences in the magnitude and morphology of polarimetric patterns. It is also possible that the scattering model does not capture some important characteristics of bat

flight, such as variability in wing position. All of these components – the behavioural model, scattering model and system characterization – can be modified and tuned until the simulated products approach those observed on KDFX. For every resolution volume, the position, velocity

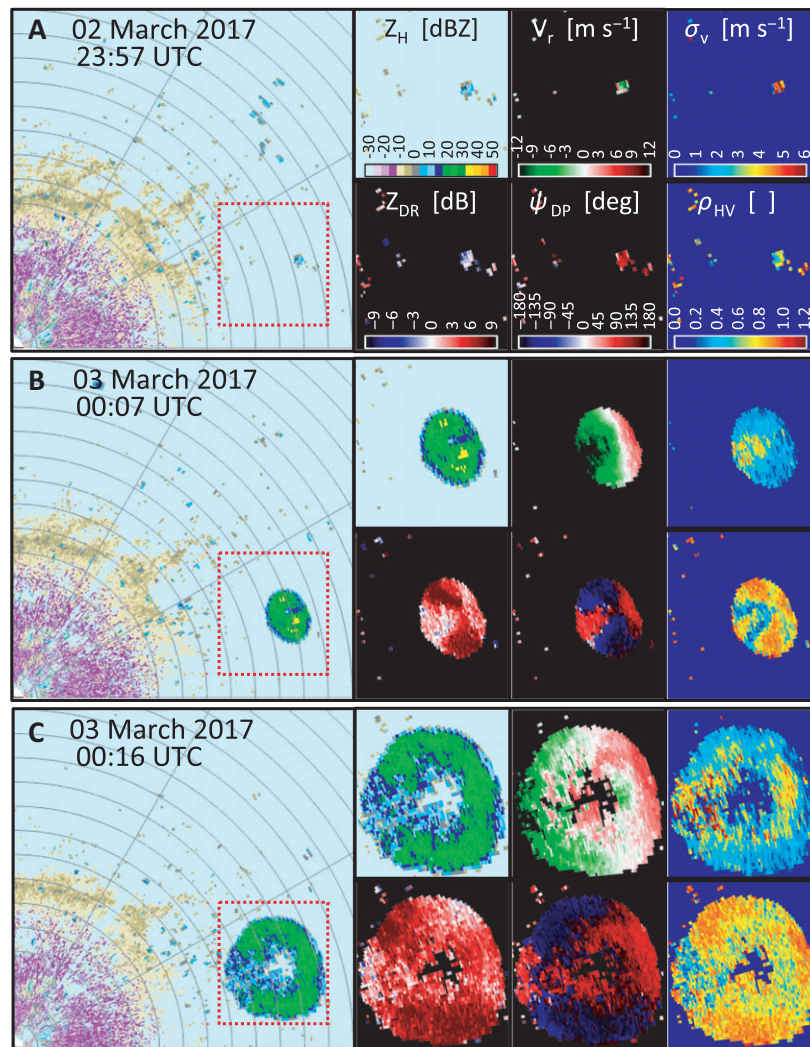


Figure 5. Radar products from the Del Rio, Texas radar (KDFX) showing the dusk emergence of Frio Cave at the 0.5° elevation sweep. The red dotted boxes indicate the domain shown in the inset images. Colour scales in (A) are valid for all subplots. Range rings are spaced at 5-km increments.

and orientation of every scatterer is known, enabling interpretation of the products with respect to animal distributions and flight behaviour. For example, the variance of agent velocities in each volume could be calculated and related to the resulting spectrum width product, providing a diagnostic link between this radar product and underlying bat flight behaviour. Such applications are an exciting future application of radar simulation schemes. Furthermore, the simulation can be replicated with different radar specifications, scan configurations or locations relative to the cave to generate ensemble comparisons. An example of this utility is demonstrated in Stepanian and Chilson (2012), which presents a single-polarization simulation of a rapid-scanning mobile radar.

Although the six radar products presented in Figure 5 are the most familiar to meteorologists and ecologists

alike, many other products and analysis techniques can be produced from the baseband data created in this simulation. Perhaps the greatest benefit of generating signals at the baseband level is the capability of developing and testing signal processing techniques. For example, time-series analysis has been used in biological applications of weather radar to identify scattering contributions of birds and insects in mixtures (Bachmann and Zrnić 2007). This unique application of power spectral density analysis uses azimuthal variability to characterize animal taxa within a uniform flow field and demonstrates the additional biological information contained within the baseband signals. Unfortunately, this Spectral Velocity Azimuth Display (SVAD) analysis is not possible using routine NEXRAD data since the baseband (i.e. Level I) data are not retained in the archive. Nonetheless, with increasing interest in

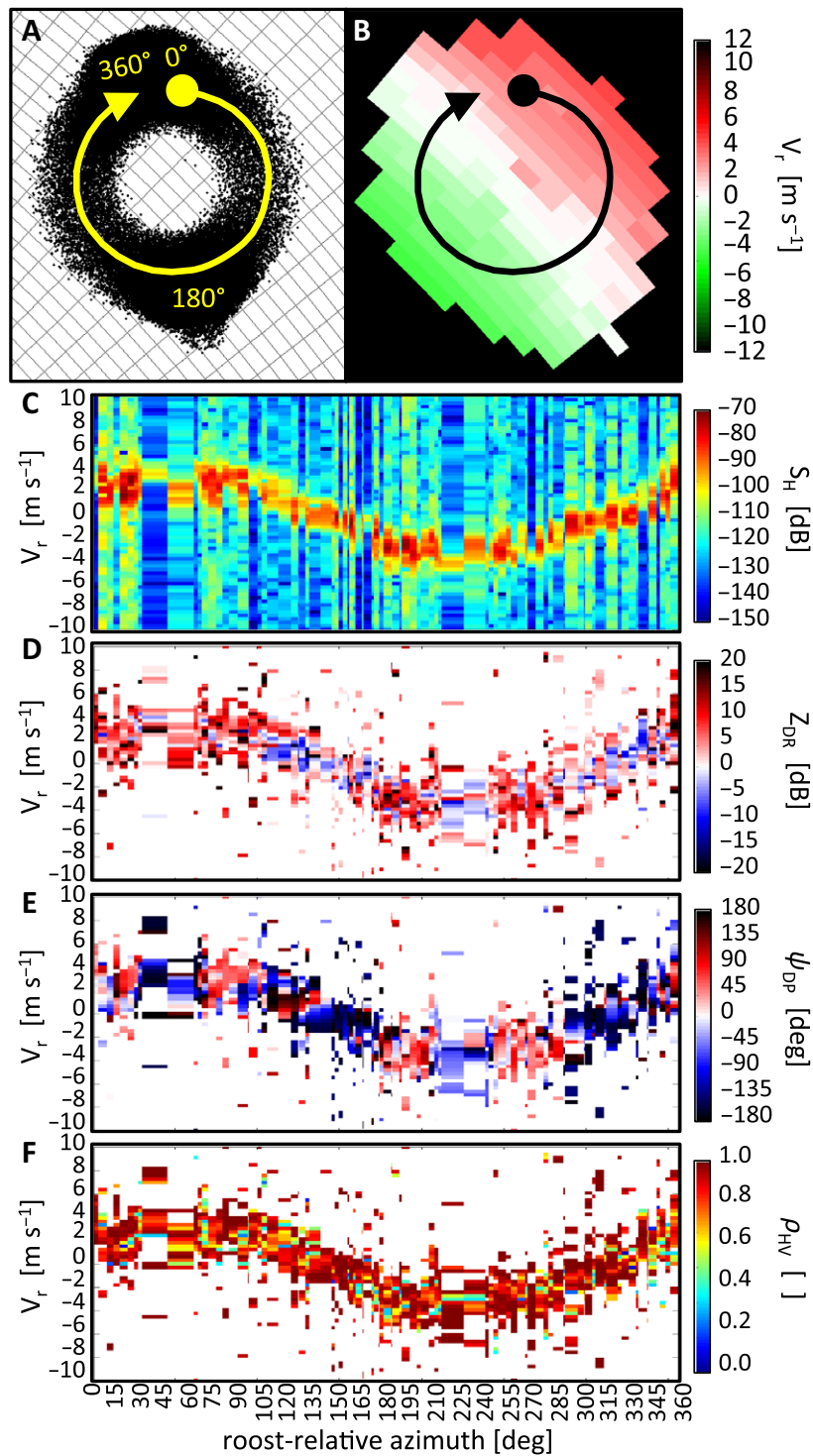


Figure 6. Development of the roost-relative spectral velocity azimuth display using the simulated baseband data. (A) Agent positions at 1200 sec (as seen in Fig. 4d) with overlaid definition of roost-relative azimuth coordinates. (B) Radial velocity at 1200 sec (as seen in Fig. 4d) with overlaid definition of roost-relative azimuth coordinates. (C) Power spectral density of pixels within the emergence ring, displayed as a function of roost-relative azimuth. (D) Spectral density of differential reflectivity for pixels within the emergence ring, displayed as a function of roost-relative azimuth. (E) Spectral density of differential phase for pixels within the emergence ring, displayed as a function of roost-relative azimuth. (F) Spectral density of copolar correlation coefficient for pixels within the emergence ring, displayed as a function of roost-relative azimuth. The tails of all spectral densities have been clipped to $\pm 10 \text{ msec}^{-1}$ to aid visualization ($V_a = \pm 25 \text{ msec}^{-1}$).

radar for animal surveillance and dedicated deployment of specialized research radars to ecologically interesting sites (Mirkovic et al. 2016), one may wonder what types of analyses could be possible if Level I data were available at sites overlooking bat caves. Investigating these theoretical capabilities is an interesting application of this simulated baseband data, and the focus of the following example.

During an emergence event, the flight behaviour of bats is not well suited for SVAD analysis because their velocities are not horizontally homogenous around the radar site. However, the SVAD principles can be modified to look at azimuthal velocity variability not around the radar site, but rather around the emergence ring. To develop this analysis technique, we define a polar coordinate system centred on the cave location (i.e. the centre of the emergence ring) with a roost-relative azimuth that increases clockwise from north (Fig. 6A). In this coordinate system, radial velocity of divergence signatures approximates the azimuthal variability of the SVAD (Fig. 6B), and baseband signals can be analysed as such. Following Bachmann and Zrnić (2007), we calculate power spectral density as well as spectral decomposition of polarimetric products for each resolution volume (i.e. pixel) in the emergence ring, and plot the resulting spectra as a function of roost relative azimuth angle (Fig. 6C–F). Note that in this coordinate system pixels are not evenly spaced in azimuth, resulting in the nonuniform azimuthal resolution in Figure 6C–F. These polarimetric spectral densities plotted in roost-relative azimuthal display highlight the divergence of bats away from the cave and highlight the dependence of polarimetric quantities on flight track, but also could enable the identification of other scatterers mixed within these resolution volumes. For example, in this display insects with zero-mean velocity would show up as a spectral band at $V_r = 0$ m sec⁻¹, and their power contributions could be quantified independently from the bats. Similarly, polarimetric variables could be sequestered by animal taxa, allowing independent characterization of the bats and the insects on which they are feeding. A full description of spectral polarimetry and its prospects in aeroecology is presented in Bachmann and Zrnić (2007).

Conclusion

Standardized observations from weather radar networks hold great potential as the foundation for automated analyses and forecasting of airborne animal movements. Just as radar observations of weather are assimilated into meteorological models, similar frameworks are a future prospect in ecology. Real-time measurements of local insect pest abundance may be used to predict dispersal distributions for the following day, or spring observations of bat

colony sizes may indicate population trends into the autumn. Ultimately, we can only speculate the applications that may evolve from coupling radar observations and modelling frameworks, but the prospects are expansive. Stakeholders in such radar research programmes are diverse – whether they be agricultural departments (Leskinen et al. 2011), civil and military aviation surveillance authorities (Dinevich and Leshem 2007), wind energy developers (Hüppop et al. 2006), environmental agencies (O'Shea and Bogan 2003; Ruth 2007) or public health officials (Bauer et al. 2017). In each application, an understanding of the link between Eulerian radar measurements and Lagrangian animal movements is important for a clear picture of the underlying ecological processes. Furthermore, radar observations can serve as a basis by which to tune ecological models, helping to identify fundamental behavioural rules on which animals act (Erni et al. 2005; Shamoun-Baranes et al. 2010; McLane et al. 2011; Shamoun-Baranes and van Gasteren 2011; Bauer and Klaassen 2013). Finally, the ability to simulate radar data from known distributions of scatterers will help ongoing efforts in developing biological radar products. For example, methods for creating 2D composites from radar volume scans or rastered mosaics from multiple radars within a network can be quantitatively assessed against the defined animal positions. In the near-term, progress in radar simulation of animal movements will require close cooperation among ecologists, meteorologists and radar engineers, with the ultimate goal of creating robust tools that can be applied by ecological modellers.

Acknowledgments

The authors thank Boon Leng Cheong, Gary McCracken and Jeff Kelly for their valuable conversations and insights at the onset of this project, as well as Judy Shamoun-Baranes and an anonymous reviewer for comments that greatly improved the final paper. Rothamsted Research is a national institute of bioscience strategically funded by the UK Biotechnology and Biological Sciences Research Council.

References

- Bachmann, S. and D. Zrnić. 2007. Spectral density of polarimetric variables separating biological scatterers in the VAD display. *J. Atmos. Oceanic Technol.* **24**, 1186–1198.
- Bauer, S. and M. Klaassen. 2013. Mechanistic models of animal migration behaviour – their diversity, structure and use. *J. Animal Ecol.* **82**, 498–508.
- Bauer, S., J. W. Chapman, D. R. Reynolds, J. A. Alves, A. M. Dokter, M. M. Menz, et al. 2017. From agricultural benefits to aviation safety: Realizing the potential of continent-wide radar networks. *BioScience*. **67**, 912–918.

- Betke, M., D. E. Hirsh, N. C. Makris, G. F. McCracken, M. Procopio, N. I. Hristov, et al. 2008. Thermal imaging reveals significantly smaller Brazilian free-tailed bat colonies than previously estimated. *J. Mammal.* **89**, 18–24.
- Bridge, E. S., K. Thorup, M. S. Bowlin, P. B. Chilson, R. H. Diehl, R. W. Fléronet al. 2011. Technology on the move: Recent and forthcoming innovations for tracking migratory birds. *BioScience*. **61**, 689–698.
- Bringi, V. N. and V. Chandrasekar. 2001. *Polarimetric Doppler weather radar: principles and applications*. 1st ed. Cambridge University Press, Cambridge.
- Byrd, A. D., I. R. Ivic, R. D. Palmer, B. M. Isom, B. L. Cheong, A. D. Schenkman, et al. 2016. A weather radar simulator for the evaluation of polarimetric phased array performance. *IEEE Trans. Geosci. Remote Sens.* **54**, 4178–4189.
- Cheong, B. L., R. D. Palmer, and M. Xue. 2008. A time series weather radar simulator based on high-resolution atmospheric models. *J. Atmos. Oceanic Technol.* **25**, 230–243.
- Chilson, P. B., W. F. Frick, J. F. Kelly, K. W. Howard, R. P. Larkin, R. H. Diehl, et al. 2012. Partly cloudy with a chance of migration: Weather, radars, and aeroecology. *Bull. Am. Meteorol. Soc.* **93**, 669–686.
- Clark, J. S. and et al. 2001. Ecological forecasts: an emerging imperative. *Science*. **293**, 657–660.
- Dinevich, L., and Y. Leshem. 2007. Algorithmic system for identifying bird radio-echo and plotting radar ornithological charts. *The Ring*. **29**, 3–40.
- Doviak, R. J. and D. S. Zrnić. 1993. *Doppler radar and weather observations*. 2nd ed. Academic Press, Cambridge, MA.
- Doviak, R. J., V. Bringi, A. Ryzhkov, A. Zahrai, and D. Zrnić. 2000. Considerations for polarimetric upgrades to operational WSR-88D radars. *J. Atmos. Oceanic Technol.* **17**, 257–278.
- Erni, B., F. Liechti, and B. Bruderer. 2005. The role of wind in passerine autumn migration between Europe and Africa. *Behav. Ecol.* **16**, 732–740.
- Frick, W. F., P. M. Stepanian, J. F. Kelly, K. W. Howard, C. M. Kuster, T. H. Kunz, et al. 2012. Climate and weather impact timing of emergence of bats. *Plos One*. **7**, 1–8.
- Gauthreaux, S. A. Jr. and C. G. Belser. 2003. Radar ornithology and biological conservation. *The Auk*. **120**, 266–277.
- Grimm, V., E. Revilla, U. Berger, F. Jeltsch, W. M. Mooij, S. F. Railsback, et al. 2005. Pattern-oriented modeling of agent-based complex systems: lessons from ecology. *Science*. **310**, 987–991.
- Hallam, T. G., A. Raghavan, D. T. Dimitrov, and P. Federico. 2006. Technology and simulation of bat population dynamics. pp. 113–117 in *Proceedings of the second IASTED International Conference on Environmental Modelling and Simulation*. St. Thomas, US Virgin Islands.
- Hobbs, S. and A. C. Aldhous. 2006. Insect ventral radar cross-section polarisation dependence measurements for radar entomology. *IEE Proc.-Radar, Sonar Navig.* **153**, 502–508.
- Horn, J. W., and T. H. Kunz. 2008. Analyzing NEXRAD doppler radar images to assess nightly dispersal patterns and population trends in Brazilian free-tailed bats (*Tadarida brasiliensis*). *Integr. Comp. Biol.* **48**, 24–39.
- Hüppop, O., J. Dierschke, K.-M. Exo, E. Fredrich, and R. Hill. 2006. Bird migration studies and potential collision risk with offshore wind turbines. *Ibis*. **148**, 90–109.
- Jung, Y., M. Xue, G. Zhang, and J. M. Straka. 2008a. Assimilation of simulated polarimetric radar data for a convective storm using the ensemble Kalman filter. Part II: Impact of polarimetric data on storm analysis. *Mon. Weather Rev.* **136**, 2246–2260.
- Jung, Y., G. Zhang, and M. Xue. 2008b. Assimilation of simulated polarimetric radar data for a convective storm using the ensemble Kalman filter. Part I: observation operators for reflectivity and polarimetric variables. *Monthly Weather Rev.* **136**, 2228–2245.
- Jung, Y., M. Xue, and G. Zhang. 2010. Simulations of polarimetric radar signatures of a supercell storm using a two-moment bulk microphysics scheme. *J. Appl. Meteorol. Climatol.* **49**, 146–163.
- Kunz, T. H., S. A. Gauthreaux, Jr., N. I. Hristov, J. W. Horn, G. Jones, E. K. V. Kalko, et al. 2008. Aeroecology: probing and modeling the aerosphere. *Integr. Comp. Biol.* **48**, 1–11.
- Lang, T. J., S. A. Rutledge, and J. L. Stith. 2004. Observations of quasi-symmetric echo patterns in clear air with the CSU-CHILL polarimetric radar. *J. Atmos. Oceanic Technol.* **21**, 182–1189.
- Leskinen, M., I. Markkula, J. Koistinen, P. Pylkko, S. Ooperi, P. Siljamo, et al. 2011. Pest insect immigration warning by an atmospheric dispersion model, weather radars and traps. *J. Appl. Entomol.* **135**, 55–67.
- McLane, A. J., C. Semeniuk, G. J. McDermid, and D. J. Marceau. 2011. The role of agent-based models in wildlife ecology and management. *Ecol. Model.* **222**, 1544–1556.
- Melnikov, V. M., M. J. Istok, and J. K. Westbrook. 2015. Asymmetric radar echo patterns from insects. *J. Atmos. Oceanic Technol.* **32**, 659–674.
1997. Department of defense world geodetic system 1984, its definition and relationships with local geodetic systems. Technical Report NIMA TR8350.2.
- Mirkovic, D., P. M. Stepanian, J. F. Kelly, and P. B. Chilson. 2016. Electromagnetic model reliably predicts radio-wave scatter from airborne organisms. *Sci. Rep.* **6**, 35637.
- Mueller, E. A. and R. P. Larkin. 1985. Insects observed using dual-polarization radar. *J. Atmos. Oceanic Technol.* **2**, 49–54.
- Muschinski, A., P. Sullivan, D. Wuertz, R. Hill, S. Cohn, D. Lenschow, and R. Doviak. 1999. First synthesis of wind-profiler signals on the basis of large-eddy simulation data. *Radio Sci.* **34**, 1437–1459.
- O'Shea, T. and M. Bogan. 2003. Monitoring trends in bat populations of the United States and territories: Problems

- and prospects. U.S. Geological Survey, Information and Technology Report 0003.
- Rapp, R. H. 1991. *Geometric geodesy, Part I. Lecture Notes*. Department of Geodetic Science and Surveying, Ohio State University, Columbus, OH.
- Reynolds, C. W. 1987. Flocks, herds, and schools: A distributed behavioral model. *Computer Graphics*. **21**, 25–34.
- Reynolds, C. W. 1999. Steering behaviors for autonomous characters. pp. 763–782 in *Proceeding of game developers conference, San Jose, California*. Miller Freeman Game Group, San Francisco, CA.
- Ruth, J. M. 2007. Applying radar technology to migratory bird conservation and management: Strengthening and expanding a collaborative. U.S. Geological Survey, Fort Collins, Colo., Open-File Report 1361.
- Ryzhkov, A. V., M. Pinsky, A. Pokrovsky, and A. Khain. 2011. Polarimetric radar observation operator for a cloud model with spectral microphysics. *J. Appl. Meteorol. Climatol.* **50**, 873–894.
- Schelleng, J., C. Burrows, and E. Ferrell. 1933. Ultra-short-wave propagation. *Proc. Radio Inst. Eng.* **21**, 427–463.
- Scipión, D. E., P. B. Chilson, E. Fedorovich, and R. D. Palmer. 2008. Evaluation of an LES-based wind profiler simulator for observations of a daytime atmospheric convective boundary layer. *J. Atmos. Oceanic Technol.* **25**, 1423–1436.
- Shamoun-Baranes, J. and H. van Gasteren. 2011. Atmospheric conditions facilitate mass migration events across the north sea. *Animal Behav.* **81**, 691–704.
- Shamoun-Baranes, J., W. Bouten, and E. E. van Loon. 2010. Integrating meteorology into research on migration. *Integr. Comp. Biol.* **50**, 280–292.
- Shamoun-Baranes, J., J. A. Alves, S. Bauer, A. M. Dokter, O. Hüppop, J. Koistinen, et al. 2014. Continental-scale radar monitoring of the aerial movements of animals. *Mov. Ecol.* **2**, 1–6.
- Skolnik, M. 2001. *Introduction to radar systems*. 3rd ed. McGraw-Hill Education, New York, NY.
- Stepanian, P. M., and P. B. Chilson. 2012. A time-series radar simulator for biological applications. pp. 25–29 in *The Seventh European Conference on Radar in Meteorology and Hydrology*. Toulouse, France.
- Stepanian, P. M., K. G. Horton, V. M. Melnikov, D. S. Zrnić, and S. A. Gauthreaux, Jr. 2016. Dual-polarization radar products for biological applications. *Ecosphere*. **7**, e01539.
- Straka, J. M., D. S. Zrnić, and A. V. Ryzhkov. 2000. Bulk hydrometeor classification and quantification using polarimetric radar data: Synthesis of relations. *J. Appl. Meteorol.* **39**, 1341–1372.
- Van Den Broeke, M. S. 2013. Polarimetric radar observations of biological scatterers in hurricanes Irene (2011) and Sandy (2012). *J. Atmos. Oceanic Technol.* **30**, 2754–2767.
- Vaughn, C. R. 1985. Birds and insects as radar targets: a review. *Proc. IEEE*. **73**, 205–227.
- Vivekanandan, J., W. Adams, and V. Bringi. 1991. Rigorous approach to polarimetric radar modeling of hydrometeor orientation distributions. *J. Appl. Meteorol.* **30**, 1053–1063.
- Wainwright, C. E., P. M. Stepanian, P. B. Chilson, R. D. Palmer, E. Fedorovich, and J. A. Gibbs. 2014. A time series sodar simulator based on large-eddy simulation. *J. Atmos. Oceanic Technol.* **31**, 876–889.
- Wilkins, K. T. 1989. *Tadarida brasiliensis*. *Mamm. Species*. **331**, 1–10.
- Wilson, J. W., T. M. Weckwerth, J. Vivekanandan, R. M. Wakimoto, and R. W. Russell. 1994. Boundary layer clear-air radar echoes: Origin of echoes and accuracy of derived winds. *J. Atmos. Oceanic Technol.* **11**, 1184–1206.
- Zrnić, D. S. 1975. Simulation of weatherlike doppler spectra and signals. *J. Appl. Meteorol. Climatol.* **14**, 619–620.
- Zrnić, D. S. and A. V. Ryzhkov. 1998. Observations of insects and birds with a polarimetric radar. *IEEE Trans. Geosci. Remote Sens.* **36**, 661–668.

Supporting Information

Additional supporting information may be found online in the supporting information tab for this article.

Video S1. Video of the full agent-based behavioral model of the dusk emergence of a cave-dwelling colony of 100,000 Brazilian free-tailed bats.

Video S2. Animated GIF of the synthesized radar products corresponding with the simulated bat emergence event.

Appendix 1. List of Symbols and Notation

Symbol	Definition
α	Euler rotation angle for agent flight yaw
β	Euler rotation angle for agent flight pitch
γ	Euler rotation angle for agent flight roll
ρ_{HV}	Copolar correlation coefficient product

(Continued)

Appendix 1. Continued.

Symbol	Definition
θ	Azimuth angle of an agent
θ_{pt}	Azimuth angle of the radar pointing direction
ϑ	Angular distance off of radar boresight
ϑ_b	One-way radar beamwidth
λ	Radar wavelength
σ_b	Radar cross section
σ_v	Spectrum width of radial velocity product
τ	Transmit pulse width
τ_s	Receiver sample time
ϕ	Elevation angle of an agent
ϕ_{pt}	Elevation angle of the radar pointing direction
ψ_s	Backscatter phase
$\psi_{t,d}$	Initial system differential phase on transmission
$\psi_{r,d}$	System differential phase shift on reception
$\psi_{t,h}$	Initial system phase in the horizontal polarization on transmission
$\psi_{t,v}$	Initial system phase in the vertical polarization on transmission
$\psi_{r,h}$	System phase shift in the horizontal polarization on reception
$\psi_{r,v}$	System phase shift in the vertical polarization on reception
$\psi_{i,vh}$	The received vertically polarized echo phase contribution from the i th agent from a horizontally polarized transmission
ψ_{DP}	Total measured differential phase product
ω_r	Antenna rotation rate
a	Earth radius
c	Speed of light
d	Distance of an agent from the radar beam boresight axis
e	Earth eccentricity
f	Antenna beam pattern
h	Height of the beam above the level of the radar
i	Index or subscript denoting a specific single agent
k_e	Equivalent Earth radius scaling parameter
n	Index or subscript denoting a specific receiver sample
r	Slant range of an agent from the radar
r_0	Centre location of a given range gate
s	Arc distance of an agent from the radar
t	Index or subscript denoting a specific single time step
x	Longitudinal distance of an agent from the radar
y	Latitudinal distance of an agent from the radar
z	Altitudinal distance of an agent above ground level
B	Receiver bandwidth
G	Antenna gain
M	Total number of time steps in the ecological model
N	Total number of agents in the ecological model
$I_i(n)$	Received in-phase echo voltage component contribution from the i th agent at the n th time sample
$Q_i(n)$	Received quadrature-phase echo voltage component contribution from the i th agent at the n th time sample
$P_{r,vh,i}(n)$	The received vertically polarized power contribution from the i th agent for the n th sample from a horizontally polarized transmission
P_t	Radar transmit power
T_s	Pulse repetition time (inverse of the pulse repetition frequency)
W	Range weighting function
$\mathbf{X}_{\text{cart}}(i, t)$	Location vector of the i th agent at the t th time step in radar-centred Cartesian coordinates $\langle x, y, z \rangle$
$\mathbf{X}_{\text{geo}}(i, t)$	Location vector of the i th agent at the t th time step in geographic coordinates $\langle \text{lat}, \text{lon}, \text{alt} \rangle$
$\mathbf{X}_{\text{geo,rad}}$	Location vector of the radar site in geographic coordinates $\langle \text{lat}_{\text{rad}}, \text{lon}_{\text{rad}}, \text{alt}_{\text{rad}} \rangle$
$\mathbf{X}_{\text{sph}}(i, t)$	Location vector of the i th agent at the t th time step in radar-centred spherical coordinates $\langle r, \phi, \theta \rangle$
$\mathbf{V}(i, t)$	Velocity vector of the i th agent at the t th time step in Cartesian coordinates $\langle u, v, w \rangle$
$\mathbf{V}_r(i, t)$	Radial velocity of the i th agent at the t th time step
$V_i(n)$	Received complex echo voltage contribution from the i th agent at the n th time sample
$V(n)$	Total received complex echo voltage at the n th time sample

(Continued)

Appendix 1. Continued.

Symbol	Definition
V_r	Radial velocity radar product
$V_H(n)$	Total received horizontally polarized complex echo voltage at the n th time sample
$V_V(n)$	Total received vertically polarized complex echo voltage at the n th time sample
Z_H	Radar reflectivity factor product for the horizontal polarization
Z_{DR}	Differential reflectivity factor product